
CURRICULUM LEARNING-DRIVEN PIELMS FOR FLUID FLOW SIMULATIONS

Vikas Dwivedi*

CREATIS Biomedical Imaging Laboratory
 INSA, CNRS UMR 5220, Inserm, Universit ´e Lyon 1
 Lyon 69621
 vikas.dwivedi@creatis.insa-lyon.fr

Bruno Sixou

CREATIS Biomedical Imaging Laboratory
 INSA, CNRS UMR 5220, Inserm, Universit ´e Lyon 1
 Lyon 69621
 bruno.sixou@insa-lyon.fr

Monica Sigovan

CREATIS Biomedical Imaging Laboratory
 INSA, CNRS UMR 5220, Inserm, Universit ´e Lyon 1
 Lyon 69621
 monica.sigovan@insa-lyon.fr

ABSTRACT

This paper presents two novel, physics-informed extreme learning machine (PIELM)-based algorithms for solving steady and unsteady nonlinear partial differential equations (PDEs) related to fluid flow. Although single-hidden-layer PIELMs outperform deep physics-informed neural networks (PINNs) in speed and accuracy for linear and quasilinear PDEs, their extension to nonlinear problems remains challenging. To address this, we introduce a curriculum learning strategy that reformulates nonlinear PDEs as a sequence of increasingly complex quasilinear PDEs. Additionally, our approach enables a physically interpretable initialization of network parameters by leveraging Radial Basis Functions (RBFs). The performance of the proposed algorithms is validated on two benchmark incompressible flow problems: the viscous Burgers equation and lid-driven cavity flow. To the best of our knowledge, this is the first work to extend PIELM to solving Burgers' shock solution as well as lid-driven cavity flow up to a Reynolds number of 100. As a practical application, we employ PIELM to predict blood flow in a stenotic vessel. The results confirm that PIELM efficiently handles nonlinear PDEs, positioning it as a promising alternative to PINNs for both linear and nonlinear PDEs.

Keywords Curriculum Learning · Navier-Stokes Equations · Physics-Informed Neural Networks · Physics-Informed Extreme Learning Machines

1 Introduction

Nonlinear partial differential equations (PDEs) play a fundamental role in fluid mechanics, governing complex phenomena in aerodynamics, weather prediction, and engineering simulations. The Navier-Stokes equations, which describe the motion of viscous fluids, are central to understanding a wide range of flow regimes. Low-speed (weakly nonlinear) flows, such as creeping flow in microfluidic devices, blood flow in large arteries, and laminar boundary layers over airfoils, are often dominated by viscous effects and exhibit smooth solutions. In contrast, high-speed (strongly nonlinear) flows, including shock waves in supersonic jets, turbulence in atmospheric dynamics, and combustion-driven flows, involve sharp gradients, discontinuities, and chaotic behavior, making them significantly harder to solve.

Traditionally, computational fluid dynamics (CFD) is based on numerical techniques such as the finite element method (Reddy, 2019) (FEM), the finite volume method (Versteeg and Malalasekera, 2007) (FVM) and spectral methods (Canuto et al., 2007). While these methods provide high accuracy, they become computationally expensive, especially for high-dimensional or highly nonlinear problems that require very fine spatial and temporal resolution.

*Corresponding Author

Property	PINN	PIELM
Hypothesis	Nonlinear in hidden layer weights	Linear in outer layer weights
Meshing	Not required	Not required
Unknowns	Weights and biases of all layers	Weights of only output layer
PDE Information	Differentiable total PDE residual	Linear system of PDE residuals
Optimization	Gradient descent	Pseudo/Matrix inverse
Applicability	Linear and nonlinear PDEs	Linear and quasi-linear PDEs
Speed	Low as compared to PIELM	High as compared to PINN

Table 1: Comparison of PINN and PIELM

To address these challenges, machine learning (ML)-based solvers have recently emerged as a promising alternative. In particular, Physics-Informed Neural Networks (Raissi et al., 2019) (PINNs) and their variants (Karniadakis et al., 2021) leverage data-driven learning while incorporating physical constraints to approximate PDE solutions efficiently. Despite their flexibility, PINNs often suffer from slow convergence, particularly for high-frequency solutions, and incur significant computational costs (Zhang et al., 2024).

To improve computational efficiency, Dwivedi and Srinivasan (Dwivedi and Srinivasan, 2020a) introduced single-hidden-layer Physics-Informed Extreme Learning Machines (PIELMs) and their distributed variant (Dwivedi et al., 2021) (DPIELM). Unlike PINNs, which optimize all network parameters through iterative backpropagation, PIELMs are linear in the outer-layer weights, allowing single-pass optimization. This significantly accelerates computations for linear PDEs (Dwivedi and Srinivasan, 2020a) (Dong and Li, 2021). PIELMs offer advantages in speed, but they also face two key challenges:

- **Limited applicability to nonlinear PDEs:** Although PIELMs outperform PINNs for linear problems, their direct extension to nonlinear PDEs remains difficult, limiting their broader applicability.
- **Lack of a systematic parameter initialization strategy:** PIELMs typically assign hidden-layer coefficients randomly within a user-defined range, making accuracy highly sensitive to these choices. However, there is no established method to select these parameters in a systematic or physically interpretable manner.

Some prior efforts have attempted to address these limitations, such as iterative nonlinear least-squares methods (Dong and Li, 2021) for handling nonlinear PDEs and differential evolution-based algorithms (Dong and Yang, 2022) for optimizing initialization. However, these methods are mathematically complex, lack physical interpretability, and have been validated only on weakly nonlinear PDEs. Although a recent study (Calabrò et al., 2021) introduced an interpretable parameter initialization method for ELM, its validation was limited to simple, steady-state, linear 1D advection-diffusion equations.

To overcome these limitations, this work proposes a curriculum learning (Bengio et al., 2009; Krishnapriyan et al., 2021) strategy, reformulating nonlinear PDEs as a sequence of quasi-linear approximations, allowing PIELMs to gradually adapt to increasing complexity. Recently, SPINNs (Ramabathiran and Ramachandran, 2021) have shown promising results in solving nonlinear PDEs by employing kernel-based neural networks with Radial Basis Functions (RBFs), offering a more interpretable formulation of the PINN hypothesis. Building on this idea, we integrate this RBF-based approach into the PIELM framework to enhance its physical interpretability.

These novelties enable classical PIELMs to efficiently tackle nonlinear fluid flows, bridging the gap between classical numerical solvers and machine learning-based approaches while maintaining computational efficiency.

Organization: The structure of this paper is outlined as follows: Section 2 briefly recaps PINNs, PIELMs, RBF methods for PDEs, and curriculum learning. Section 3 presents the proposed methodology. Section 4 discusses the results on Burgers’ equation, lid-driven cavity flow and stenotic flow, and Section 5 concludes with key findings and future directions.

2 Background

PINNs In a typical Physics-Informed Neural Network (PINN) framework, a deep neural network approximates the solution of PDEs. Randomly distributed collocation points within the computational domain, along with boundary points, serve as the training dataset. At these points, penalties are introduced for deviations from the governing PDE and boundary conditions (BCs). The mean squared error of these penalties, representing the residuals of the PDE and BCs, defines a physics-based loss function. This loss is minimized using gradient descent-based optimization algorithms

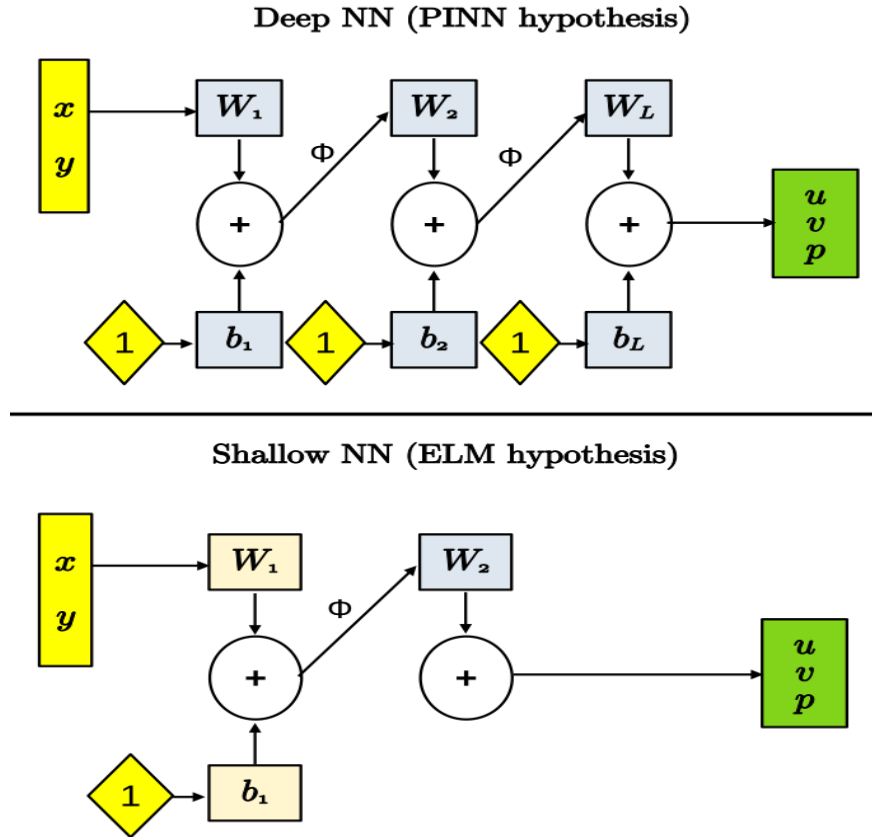


Figure 1: Comparison of Network Architectures: PINN vs. PIELM. The figure illustrates the differences between deep PINNs (where all weights are trainable) and single-layer PIELMs (where input weights remain fixed). Yellow and green blocks indicate the input (spatial variables) and output (flow variables) of the networks. Network parameters, i.e. weights and biases, are denoted as W_i and b_i . Trainable parameters are shown in gray, while the fixed input layer parameters of PIELM are highlighted in light orange.

and backpropagation. The core idea behind PINNs and their variants is to reformulate the task of solving PDEs as an optimization problem driven by a physics-informed loss function.

PIELMs Physics-Informed Extreme Learning Machine (PIELM) differs from PINN in two key aspects: (A) network architecture and (B) cost function minimization. Unlike the deep multilayer architecture of PINNs, PIELM employs a single-hidden-layer design. A distinctive feature of PIELM is that its input layer weights are randomly initialized and remain fixed during training. With the first layer weights held constant, the PDE solution becomes linear with respect to the output layer weights, making the approximation process inherently linear. Instead of minimizing a physics-informed loss function through computationally intensive gradient descent and backpropagation techniques, PIELM formulates a system of linear residual equations, which can be efficiently solved using matrix inversion. Figure 1 compares the PINN and PIELM hypotheses for solving the Navier-Stokes equations. Table 1 provides a detailed comparison of their key properties.

RBF Methods for PDEs Radial Basis Function (RBF) kernels (Buhmann, 2000) are popular for solving PDEs due to their flexibility and ability to model complex, multidimensional problems. These real-valued functions depend on the distance between points, making them ideal for interpolating scattered data. Common RBFs, such as Gaussian, multi-quadric, and inverse multi-quadric, are parameterized to control smoothness and influence radius. In the context of PDEs, RBFs approximate solutions by constructing a weighted sum of basis functions centered at collocation points, which satisfy the governing equations and boundary conditions (Kansa, 1990a,b). This approach is computationally efficient, as it avoids iterative optimization, but the performance is heavily dependent on the careful selection of kernel parameters (Fasshauer and Zhang, 2007) and collocation points.

Curriculum Learning Curriculum learning (Bengio et al., 2009; Bengio, 2009) is a machine learning strategy where a model is trained by presenting examples in a sequence of increasing difficulty, similar to how humans learn. The idea is to start with simpler, easier-to-learn tasks and gradually progress to more complex ones. This approach helps the model to converge more efficiently by providing a structured learning path, avoiding early confusion with overly difficult examples (Elman, 1993). Curriculum learning has been successfully applied in various fields, such as reinforcement learning (Parisotto and Salakhutdinov, 2017), natural language processing (Campos, 2021), and computer vision (Wang et al., 2024), where it has been shown to improve the training stability, convergence rate, and generalization performance of models.

3 Methods

3.1 Test Cases

To evaluate the performance of PIELM, we have selected two standard nonlinear PDEs from fluid dynamics: (1) Burgers' equation and (2) Navier-Stokes equations.

3.1.1 Burgers' Equation

Burgers' equation models nonlinear advection with linear diffusion, and is expressed as follows:

$$\frac{\partial u}{\partial t} + u \frac{\partial u}{\partial x} = \nu \frac{\partial^2 u}{\partial x^2}, \quad (x, t) \in \Omega \quad (1)$$

where:

- $u : \Omega \rightarrow \mathbb{R}$ is the velocity field,
- $x \in \mathbb{R}$ is the spatial coordinate,
- $t \in \mathbb{R}$ is time,
- $\nu \in \mathbb{R}$ is the viscosity coefficient,
- $\Omega \subset \mathbb{R}^2$ represents the spatio-temporal computational domain (rectangle in (x, t)).

The equation describes the balance between the nonlinear advection term $u \frac{\partial u}{\partial x}$ and the linear diffusion term $\nu \frac{\partial^2 u}{\partial x^2}$. For small values of ν , the solution exhibits sharp gradients, and as $\nu \rightarrow 0$, the solution may develop discontinuities, commonly referred to as shocks. These properties make Burgers' equation particularly useful for modeling abrupt changes in flow behavior.

3.1.2 Navier-Stokes Equations

The Navier-Stokes equations describe the motion of viscous fluid substances. We restrict here to steady-state solutions. The steady-state, incompressible form of these equations in two dimensions is expressed as:

$$\nabla \cdot \vec{V} = 0, \quad (x, y) \in \Omega \quad (2)$$

$$(\vec{V} \cdot \nabla) \vec{V} = -\nabla p + \frac{1}{Re} \nabla^2 \vec{V}, \quad (x, y) \in \Omega \quad (3)$$

where:

- $\vec{V} = \begin{pmatrix} u \\ v \end{pmatrix} : \Omega \rightarrow \mathbb{R}^2$ is the velocity field,
- $u, v \in \mathbb{R}$ are the velocity components in the x - and y -directions, respectively,
- $p : \Omega \rightarrow \mathbb{R}$ is the pressure field,
- $Re \in \mathbb{R}$ is the Reynolds number,
- ∇ and ∇^2 denote the gradient and Laplacian operators, respectively,
- $\Omega \subset \mathbb{R}^2$ represents the 2D computational domain, and $\partial\Omega$ is its boundary.

Equation 2 describes mass conservation, while Equation 3 represents momentum conservation in the horizontal and vertical directions. The left side of the momentum equation contains the inertial terms, while the right side contains the pressure term and the viscous term. The balance between the inertia and viscous forces determines the flow behavior. The Reynolds number (Re) characterizes the ratio of inertia to viscous forces: high values of Re correspond to turbulent flows, while low values indicate viscosity-dominated slow flows. Practically, the Reynolds number is defined as:

$$Re = \frac{UL}{\nu}$$

where L is the characteristic length, U is the characteristic velocity and ν is the kinematic viscosity. The pressure term primarily ensures mass conservation.

3.2 Proposed Curriculum Learning for Nonlinear PDEs

Curriculum learning (Bengio et al., 2009) follows a progression from simpler concepts to more complex ones. When applied to solving PDEs, this approach involves first solving simpler PDEs before moving on to more complex ones (Krishnapriyan et al., 2021). PIELMs have shown promising results in solving linear and quasi-linear PDEs. However, their inherently linear formulation prevents their direct application to nonlinear problems. We introduce curriculum learning-based algorithms for solving both unsteady and steady nonlinear PDEs. While the ideas are general, we explain them in the context of our test cases: Burgers' equation for unsteady problems and the Navier-Stokes equations for steady cases.

3.2.1 For Burgers' Equation

The nonlinear advection term $u \frac{\partial u}{\partial x}$ in Burgers' equation 1 is the main modeling challenge for PIELM which is based on a linear representation of the solution. To address this, we approximate it using a quasi-linear formulation. However, the accuracy of this linearized model is generally limited to small deviations from the chosen linearization point. To overcome this limitation, rather than solving the PDE over the entire computational domain at once, we partition the domain into multiple time blocks and solve the linearized Burgers' equation sequentially using a predictor-corrector approach.

Assume that we partition the computational domain $\Omega = [0, T] \times [-1, 1]$ into B time blocks such that:

$$\Omega = \bigcup_{i=0}^{B-1} \Omega_i, \quad \text{where } \Omega_i = [i \cdot dT, (i+1) \cdot dT] \times [-1, 1], \quad i = 0, 1, 2, \dots, B-1,$$

with each block Ω_i corresponding to the time interval $[i \cdot dT, (i+1) \cdot dT]$, where dT is the time step size, and $T = B \cdot dT$ is the total time. In the first time block ($B = 1$), the linearization point is set by the initial condition. We first solve the predictor step, where the linearized Burgers' equation is solved using the initial condition as the reference velocity:

$$u_{pred} = u(x, t = 0) \tag{4}$$

$$\frac{\partial u}{\partial t} + u_{pred} \frac{\partial u}{\partial x} = \nu \frac{\partial^2 u}{\partial x^2} \tag{5}$$

Next, in the corrector step, we refine the solution by solving the linearized equation again, using the predictor solution ($\hat{u}_{B=1}(x, t)$) as the updated reference:

$$u_{corr} = \hat{u}_{B=1}(x, t) \tag{6}$$

$$\frac{\partial u}{\partial t} + u_{corr} \frac{\partial u}{\partial x} = \nu \frac{\partial^2 u}{\partial x^2} \tag{7}$$

This iterative predictor-corrector process is applied across all time blocks. The full pseudocode for this procedure is presented in Algorithm 1.

3.2.2 For Navier-Stokes Equation

Similar to Burgers' equation, the nonlinear advection term $(\vec{V} \cdot \nabla) \vec{V}$ in the Navier-Stokes equations is the main problem for PIELM. To address this, we adopt a quasi-linear approximation. However, unlike Burgers' equation, a steady problem cannot be decomposed into spatial blocks, nor do we have a predefined reference solution, such as an initial condition, for linearization.

Algorithm 1 Curriculum learning-based PIELM for Burgers' equation

```

1: Initialize  $B \leftarrow 0$ ,  $u(x, t_{init}) \leftarrow F_{ic}(x)$ 
2: Approximate  $uu_x \leftarrow u(x, t_{init})u_x$ 
3: Solve Burgers equations with quasi-linear advection terms (predictor-step)
4: Approximate  $uu_x$  using  $u$  from predictor-step.
5: Solve Burgers equations with quasi-linear advection terms (corrector-step)
6:  $B \leftarrow B + 1$ 
7:  $u(x, t_{init})_B \leftarrow (u(x, t_{end}))_{B-1}$ 
8: while  $B \leq B_{target}$  do
9:   Approximate  $uu_x \leftarrow u(x, t_{init})u_x$ 
10:  Solve Burgers equations with quasi-linear advection terms (predictor-step)
11:  Approximate  $uu_x$  using  $u$  from predictor-step.
12:  Solve Burgers equations with quasi-linear advection terms (corrector-step)
13:   $B \leftarrow B + 1$ 
14:   $u(x, t_{init})_B \leftarrow (u(x, t_{end}))_{B-1}$ 
15: end while

```

To resolve this, we initially set $(\vec{V} \cdot \nabla) \vec{V} = \vec{0}$ and use the Stokes flow solution as the starting linearization point. The PIELM solution for Stokes flow serves as the initial condition, and for the quasi-linear approximation. Instead of progressing through time blocks, we advance incrementally in Reynolds number (Re). The complete pseudocode for this approach is provided in Algorithm 2.

Algorithm 2 Curriculum learning-based PIELM for Navier-Stokes equations

```

1: Initialize  $Re \leftarrow 0$ ,  $\delta \leftarrow \delta_{user}$ 
2: Solve Navier-Stokes equations ignoring advection terms (Stokes flow)
3: Approximate  $(\mathbf{V} \cdot \nabla) \mathbf{V} \leftarrow (\mathbf{V}_{Stokes} \cdot \nabla) \mathbf{V}$ 
4: Solve Navier-Stokes equations including quasi-linear advection terms
5:  $Re \leftarrow Re + \delta$ 
6: while  $Re \leq Re_{target}$  do
7:   Approximate  $(\mathbf{V} \cdot \nabla) \mathbf{V} \leftarrow (\mathbf{V}_{Re-\delta} \cdot \nabla) \mathbf{V}$ 
8:   Solve Navier-Stokes equations with quasi-linear advection terms
9:    $Re \leftarrow Re + \delta$ 
10: end while

```

3.3 PIELM Formulation

We present a formulation based on the Navier-Stokes equations. The computational domain is two-dimensional for both the Burgers equations and the Navier-Stokes equations, with (x, t) coordinates for Burgers and (x, y) for Navier-Stokes. Consequently, the interpretation of the PIELM input parameters will remain unchanged. However, while the PIELM output for the Burgers equation is a scalar u , it is a vector (u, v, p) for the Navier-Stokes equations. Therefore, the reader can derive the formulation for the Burgers equation as a special case of the Navier-Stokes equations.

3.3.1 Hypothesis

Consider two column vectors, $\vec{\alpha}^*$ and $\vec{\beta}^*$, which represent the x - and y -coordinates of the centers of the RBF kernel, respectively. In addition, we define two scaling vectors, \vec{m} and \vec{n} , which scale the coordinates along the x - and y -directions, respectively. Now, we define new vectors $\vec{\alpha}$ and $\vec{\beta}$ by performing element-wise multiplication of the scaling vectors \vec{m} and \vec{n} with $\vec{\alpha}^*$ and $\vec{\beta}^*$, respectively. Specifically, the vectors $\vec{\alpha}$ and $\vec{\beta}$ are given by:

$$\vec{\alpha} = \vec{m} \odot \vec{\alpha}^*, \quad \vec{\beta} = \vec{n} \odot \vec{\beta}^*,$$

where \odot denotes element-wise multiplication (also known as the Hadamard product). Then, the set of vectors $(\vec{\alpha}, \vec{\beta}, \vec{m}, \vec{n})$ constitute the parameters of the input layer of ELM. In the ELM architecture, the input layer parameters are user-selected and not trainable. Consequently, the output is expressed as a linear combination of the outer layer weights.

For 2D steady Navier-Stokes equations, the hypothesis of proposed PIELM (refer Figure1) is given by

$$\hat{u}(x, y) = \sum_{k=1}^{k=N^*} \phi(z_k(x, y))c_{u,k} \quad (8)$$

$$\hat{v}(x, y) = \sum_{k=1}^{k=N^*} \phi(z_k(x, y))c_{v,k} \quad (9)$$

$$\hat{p}(x, y) = \sum_{k=1}^{k=N^*} \phi(z_k(x, y))c_{p,k} \quad (10)$$

where $\vec{c} = \begin{pmatrix} \vec{c}_u \\ \vec{c}_v \\ \vec{c}_p \end{pmatrix}$ denotes outer layer weights (W_2 of PIELM hypothesis in Figure1), N^* denotes the number of neurons in the hidden layer, ϕ is the radial basis function defined by $\phi(z) = e^{-z^2}$, and $z_k(x, y)$ is given by

$$z_k(x, y) = \sqrt{(m_k x + \alpha_k)^2 + (n_k y + \beta_k)^2} \quad (11)$$

where $(m_k, n_k, \alpha_k, \beta_k)$ denote elements of $(\vec{m}, \vec{n}, \vec{\alpha}, \vec{\beta})$. The input layer parameters for (u, v, p) are kept same to respect the pressure-velocity coupling.

Suppose that we define $\xi = -z^2$. Then the expressions for the first derivative terms are as follows:

$$\frac{\partial \hat{u}}{\partial x} = \sum_{k=1}^{k=N^*} \frac{\partial \phi}{\partial \xi_k} \frac{\partial \xi_k}{\partial x} c_{u,k} = \sum_{k=1}^{k=N^*} -2e^{\xi_k} m_k (m_k x + \alpha_k) c_{u,k} \quad (12)$$

$$\frac{\partial \hat{u}}{\partial y} = \sum_{k=1}^{k=N^*} \frac{\partial \phi}{\partial \xi_k} \frac{\partial \xi_k}{\partial y} c_{u,k} = \sum_{k=1}^{k=N^*} -2e^{\xi_k} n_k (n_k y + \beta_k) c_{u,k} \quad (13)$$

Similarly, we can derive expressions for the remaining first derivative terms $\left(\frac{\partial v}{\partial x}, \frac{\partial v}{\partial y}\right)$ and $\left(\frac{\partial p}{\partial x}, \frac{\partial p}{\partial y}\right)$ by multiplying with corresponding outer layer weights for v and p respectively.

The second derivative terms are given as follows:

$$\frac{\partial^2 \hat{u}}{\partial x^2} = \sum_{k=1}^{k=N^*} -2e^{\xi_k} m_k^2 \{1 - 2(m_k x + \alpha_k)^2\} c_{u,k} \quad (14)$$

$$\frac{\partial^2 \hat{u}}{\partial y^2} = \sum_{k=1}^{k=N^*} -2e^{\xi_k} n_k^2 \{1 - 2(n_k y + \beta_k)^2\} c_{u,k} \quad (15)$$

The expressions for $\left(\frac{\partial^2 v}{\partial x^2}, \frac{\partial^2 v}{\partial y^2}\right)$ can be derived by multiplying with corresponding outer layer weights for v .

3.3.2 Interpretation of PIELM Parameters

The proposed formulation, inspired by SPINN (Ramabathiran and Ramachandran, 2021), enables a physically interpretable initialization of network parameters by leveraging the properties of Radial Basis Functions (RBFs). Unlike random initialization methods, we directly associate the input layer parameters of the PIELM with meaningful physical quantities—specifically, the locations and characteristic scales of Gaussian functions.

The 2D Gaussian function, parameterized by mean and standard deviation vectors, is given by:

$$G(x, y; \alpha^*, \beta^*, \sigma_x, \sigma_y) = e^{-\left(\frac{(x-\alpha^*)^2}{2\sigma_x^2} + \frac{(y-\beta^*)^2}{2\sigma_y^2}\right)}. \quad (16)$$

On comparing this to the equation 11, we can deduce that the input layer parameters of the ELM $(\vec{\alpha}, \vec{\beta}, \vec{m}, \vec{n})$ correspond to

$$\left(-\frac{1}{\sqrt{2}\sigma_x^*} \vec{\alpha}^*, -\frac{1}{\sqrt{2}\sigma_y^*} \vec{\beta}^*, \frac{1}{\sqrt{2}\sigma_x^*}, \frac{1}{\sqrt{2}\sigma_y^*}\right). \quad (17)$$

Here, $(\vec{\alpha}^*, \vec{\beta}^*)$ represent the spatial locations of the RBF centers, which are physically meaningful parameters that should be sampled from within the computational domain Ω . Likewise, (\vec{m}, \vec{n}) represents the reciprocal of $(\vec{\sigma}_x, \vec{\sigma}_y)$, which controls the spread of the activation functions. A structured flowchart outlining the process for selecting input layer parameters is presented below:

1. Start
2. Define Computational Domain (Ω)
 - Identify the spatial boundaries and physical constraints of the problem.
3. Determine RBF Centers (α^*, β^*)
 - Sample spatial locations of RBF centers within Ω .
 - Ensure distribution aligns with physical characteristics of the domain (e.g., more centers near walls).
4. Define Characteristic Lengths (L_c)
 - Establish relevant length scales for the problem.
5. Determine Standard Deviations (σ_x, σ_y)
 - Adjust based on sharp gradients:
 - For Burgers' equation: Concentrate sharp RBF kernels (smaller σ) near steep gradients.
 - For lid-driven cavity or stenotic flow: Concentrate sharp RBF kernels near walls or constriction.
6. Compute Input Layer Parameters
 - $\alpha = -\frac{1}{\sqrt{2}\sigma_x}\alpha^*$
 - $\beta = -\frac{1}{\sqrt{2}\sigma_y}\beta^*$
 - $m = \frac{1}{\sqrt{2}\sigma_x}$
 - $n = \frac{1}{\sqrt{2}\sigma_y}$
7. Initialize ELM with Computed Parameters
8. End

For specific cases, such as lid-driven cavity flow, a single characteristic length is sufficient, e.g., the distance between the cavity center and its corner. However, in more complex geometries, multiple length scales may be needed. For example, in a stenotic blood flow simulation, one length scale could be the inlet/outlet diameter, while another could represent the constriction diameter.

The proposed strategy bridges the gap between physics and machine learning, ensuring that the network's initial parameters have a well-grounded physical interpretation.

3.3.3 Residuals

1. *PDE residual*: For each collocation point within Ω , we calculate residuals from continuity, x and y - momentum equations and set them equal to zero as follows:

$$M\vec{c} = \vec{0} \quad (18)$$

where M is a block matrix and \vec{c} is outer layer weights matrix. Specifically,

$$\begin{bmatrix} M_{u1} & M_{v1} & M_{p1} \\ M_{u2} & M_{v2} & M_{p2} \\ M_{u3} & M_{v3} & M_{p3} \end{bmatrix} \begin{pmatrix} \vec{c}_u \\ \vec{c}_v \\ \vec{c}_p \end{pmatrix} = \begin{pmatrix} 0 \\ 0 \\ 0 \end{pmatrix} \quad (19)$$

Here the shape of individual blocks is $1 \times N^*$. The first row corresponds to the continuity equation. The second and third rows correspond to the x and y - momentum equations, respectively. For $k = 1, 2, \dots, N^*$,

$$M_{u1}(1, k) = -2e^{\xi_k} m_k (m_k x + \alpha_k) \quad (20)$$

$$M_{v1}(1, k) = -2e^{\xi_k} n_k (n_k y + \beta_k) \quad (21)$$

$$M_{p1}(1, k) = 0 \quad (22)$$

$$M_{u2}(1, k) = \hat{u}_{ref} M_{u1}(1, k) + \hat{v}_{ref} M_{v1}(1, k) + \frac{2e^{\xi_k}}{Re} [m_k^2 \{1 - 2(m_k x + \alpha_k)^2\} + n_k^2 \{1 - 2(n_k y + \beta_k)^2\}] \quad (23)$$

$$M_{v2}(1, k) = 0 \quad (24)$$

$$M_{p2}(1, k) = M_{u1}(1, k) \quad (25)$$

$$M_{u3}(1, k) = 0 \quad (26)$$

$$M_{v3}(1, k) = M_{u2}(1, k) \quad (27)$$

$$M_{p3}(1, k) = M_{v1}(1, k) \quad (28)$$

The terms \hat{u}_{ref} and \hat{v}_{ref} represent the reference velocities used in the quasi-linear approximation of the nonlinear advection terms, as previously discussed.

2. *Boundary condition residual*: For each boundary point in $\partial\Omega$, we can express the residual depending on the type of boundary condition (Dirichlet, Neumann, or mixed). For example, the expression for no-slip condition is as follows:

$$\begin{bmatrix} B_{u1} & B_{v1} & B_{p1} \\ B_{u2} & B_{v2} & B_{p2} \end{bmatrix} \begin{pmatrix} \vec{c}_u \\ \vec{c}_v \\ \vec{c}_p \end{pmatrix} = \begin{pmatrix} 0 \\ 0 \end{pmatrix} \quad (29)$$

For $k = 1, 2, \dots, N^*$,

$$B_{u1}(1, k) = e^{\xi_k} \quad (30)$$

$$B_{v1}(1, k) = 0 \quad (31)$$

$$B_{p1}(1, k) = 0 \quad (32)$$

$$B_{u2}(1, k) = 0 \quad (33)$$

$$M_{v2}(1, k) = B_{u1}(1, k) \quad (34)$$

$$M_{p2}(1, k) = 0 \quad (35)$$

Similarly, the expression for velocity inlet along horizontal direction can be written by modifying the RHS term to $\begin{pmatrix} U(y) \\ 0 \end{pmatrix}$.

3.3.4 Optimization

On assembling all the residuals, we typically get an over-determined system of linear equations of the form

$$\mathbf{A} \vec{c} = \vec{b}. \quad (36)$$

The least square solution of \vec{c} is found via least squares approach, i.e.,

$$\vec{c} = \text{pinv}(\mathbf{A}) \vec{b} \quad (37)$$

where *pinv* refers to pseudo-inverse. This approach is much faster than back propagation-based gradient descent algorithms.

4 Results and Discussion

In this section, we:

1. Evaluate the performance of PIELM and PINN for solving the linear 2D Poisson equation, showing that PIELM surpasses PINN in both computational efficiency and accuracy.
2. Demonstrate, for the first time in the literature, that PIELM effectively captures shocks in the viscous Burgers' equation rapidly and with only half the training parameters required by PINN.
3. Extend PIELM to solve the steady Navier-Stokes equations for the lid-driven cavity benchmark problem, achieving accurate solutions for Reynolds numbers up to 100.
4. Apply PIELM to simulate stenotic blood flow at various Reynolds numbers as a real-world application.

	PINN	PIELM
Data points	13657	1905
Parameters	5301	2000
Activation	\tanh	\tanh
L_2 Error	$\sim 1e-1$	$\sim 1e-5$
Time taken	97 s	0.5 s

Table 2: PINN vs PIELM for linear 2D Poisson’s equation

We also emphasize that this paper is intended as a proof-of-concept study, and therefore, we have not performed a comprehensive analysis of hyperparameter selection. In particular, we do not present dedicated hyperparameter selection studies on the influence of the number and distribution of sampling points, the placement and spread of RBF centers, or the effects of time step and Reynolds number increments. A thorough investigation into hyperparameter tuning and optimization is beyond the scope of this work and will be explored in future studies.

All the experiments are conducted in Matlab R2022b environment running in a 12th Gen Intel(R) Core(TM) i7-12700H, 2.30 GHz CPU and 16GB RAM Asus laptop.

4.1 Poisson’s Equation - PIELM versus PINN

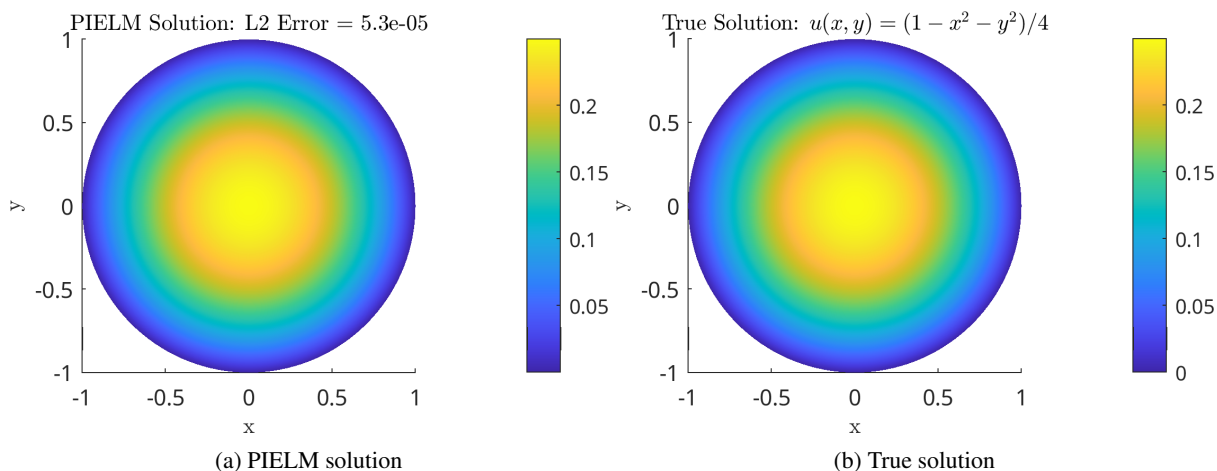


Figure 2: PIELM solution for Poisson’s equation

We refer to the Poisson equation test case published by MATLAB’s official documentation². We consider MATLAB’s PINN solution as a reference and solve the same problem with PIELM.

- **Problem Description:** $-\left(\frac{\partial^2 u}{\partial x^2} + \frac{\partial^2 u}{\partial y^2}\right) = 1$ in Ω , $u = 0$ on $\delta\Omega$, where Ω is the unit disk. The exact solution is $u(x,y) = (1 - x^2 - y^2)/4$
- **Result:** Figure 2 presents the results obtained using PIELM for this problem, while Table 2 provides a comparison with PINN. Similar to PINNs, there is no well defined formula for selecting the optimal number of neurons in the hidden layer, as discussed in previous studies (Dwivedi and Srinivasan, 2020a,b; Dong and Yang, 2022). However, unlike traditional numerical methods, where truncation error can be systematically reduced, the error in PIELM solutions does not necessarily converge to zero by merely increasing the number of hidden-layer neurons. In this test case, we used fewer than half the number of parameters compared to PINN and only a small fraction of the data points. The results confirm that PIELM surpasses PINN in both speed and accuracy as a linear solver.

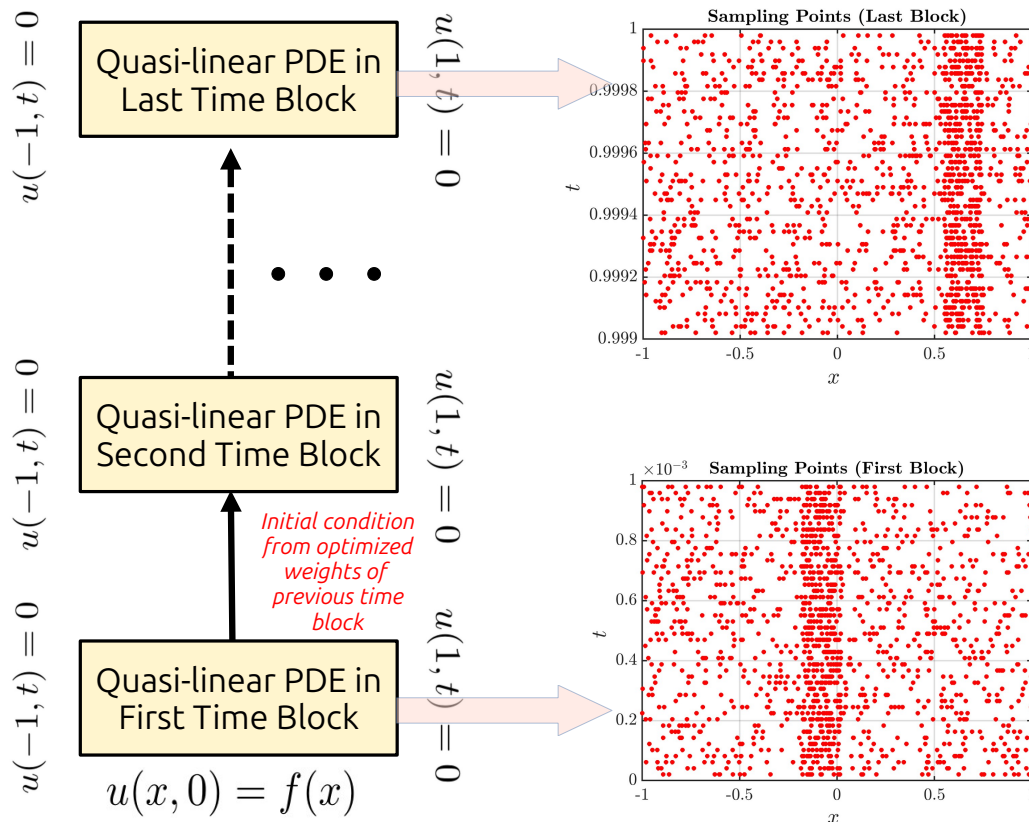


Figure 3: (Left) Time-marching strategy for solving Burgers' equation. (Right) Example of RBF kernel distribution for the first and last time blocks, assuming a traveling wave initial condition $f(x) = e^{-30x^2}$. Higher kernel density is used near regions with steep gradients in the initial condition of the time block.

4.2 Burgers' Equation

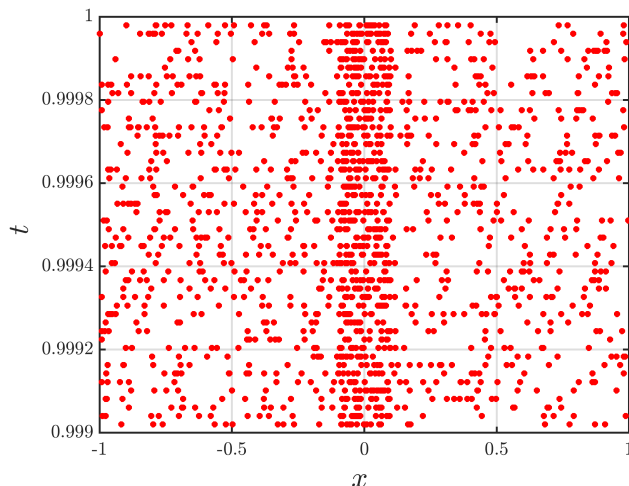
We solve Burgers' equation 1 over the computational domain $[-1, 1] \times [0, 1]$ with a small viscosity parameter $\nu = 0.01/\pi$. The Dirichlet boundary conditions are given by $u(-1, t) = 0$ and $u(1, t) = 0$. We consider two types of initial conditions:

1. A Gaussian hump, which evolves into a traveling shock solution.
2. A sine wave, which results in a standing shock solution.

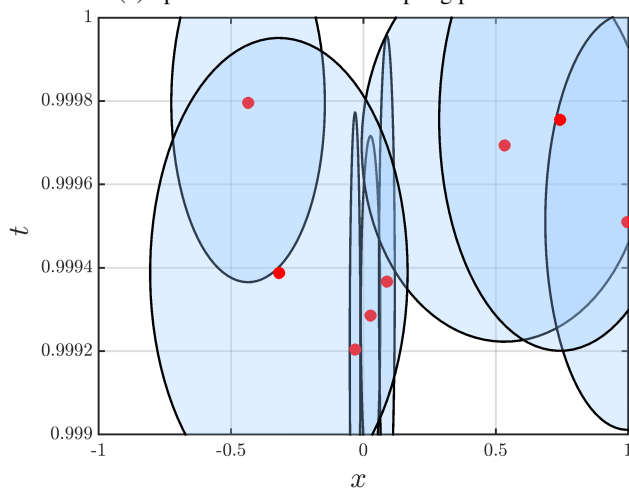
PIELM employs a time-marching strategy to solve Burgers' equation, where the optimal weights from the previous time block initialize the current block. The gradient of the initial condition is computed to identify regions with steep variations. To effectively capture shocks, a small traveling window is defined, and the absolute sum of gradients within this window is evaluated. The window with the highest gradient sum is identified, and sampling points are concentrated in this region to enhance resolution. Additionally, the standard deviation of RBF kernels in this high-gradient region is kept smaller compared to the rest of the computational domain, improving local approximation accuracy.

In this study, the traveling window size is set to 0.1, with 30% of the total collocation points allocated within this region. For the standing shock case, the high-gradient region remains fixed at the center, whereas for the traveling shock case, the shock position continuously shifts. The sampling point distribution for the traveling shock case is illustrated in Figure 3. The figure demonstrates that a higher density of RBF kernels is placed in regions with steep initial condition gradients. Figure 4 provides a visualization of the spatial variation of the standard deviations of the RBF kernel, showing

²<https://fr.mathworks.com/help/pde/ug/solve-poisson-equation-on-unit-disk-using-pinn.html>



(a) Spatial distribution of sampling points.



(b) Spatial variation of RBF kernel standard deviations.

Figure 4: Visualization of sampling points and the spatial variation of RBF kernel standard deviations.

that the spread of the RBF kernels in high-gradient regions is narrower than in other areas. Mathematically,

$$\sigma_x^{(j)} = \begin{cases} \text{Uniform}(0.01, 0.04), & \text{if } x_L \leq \alpha_j^* \leq x_R, \\ \text{Uniform}(0.02, 0.6), & \text{otherwise.} \end{cases}$$

Here, x_L and x_R define the high-gradient region, and "uniform" refers to a uniform random distribution. The standard deviations inside and outside the shock region are chosen based on corresponding length scales. For σ_t , relatively larger values (0.4-0.6 times the time step size) are selected. It should be noted that the physical interpretation of the PIELM parameters enables the selection of their ranges based on both physical and geometrical aspects of the problem.

The details of the PIELM solution for the standing and traveling shock cases are summarized in Table 3 and the results are shown in Figures 5 and 6. PIELM successfully captures both types of shock solutions, demonstrating its effectiveness. For comparison with PINN, we refer to the official documentation of MATLAB³, which presents a PINN-based solution for the viscous shock test case. The PINN implementation utilizes a second-order optimizer and the high-performance `dlaccelerate`⁴ training routine, achieving accurate results with 3000 parameters in 15 minutes. In particular, PIELM produces comparable results with only 1500 learning parameters, highlighting its computational efficiency.

³<https://fr.mathworks.com/help/deeplearning/ug/solve-partial-differential-equations-with-lbfgs-method-and-deep-learning.html>

⁴<https://fr.mathworks.com/help/deeplearning/ref/dlaccelerate.html>

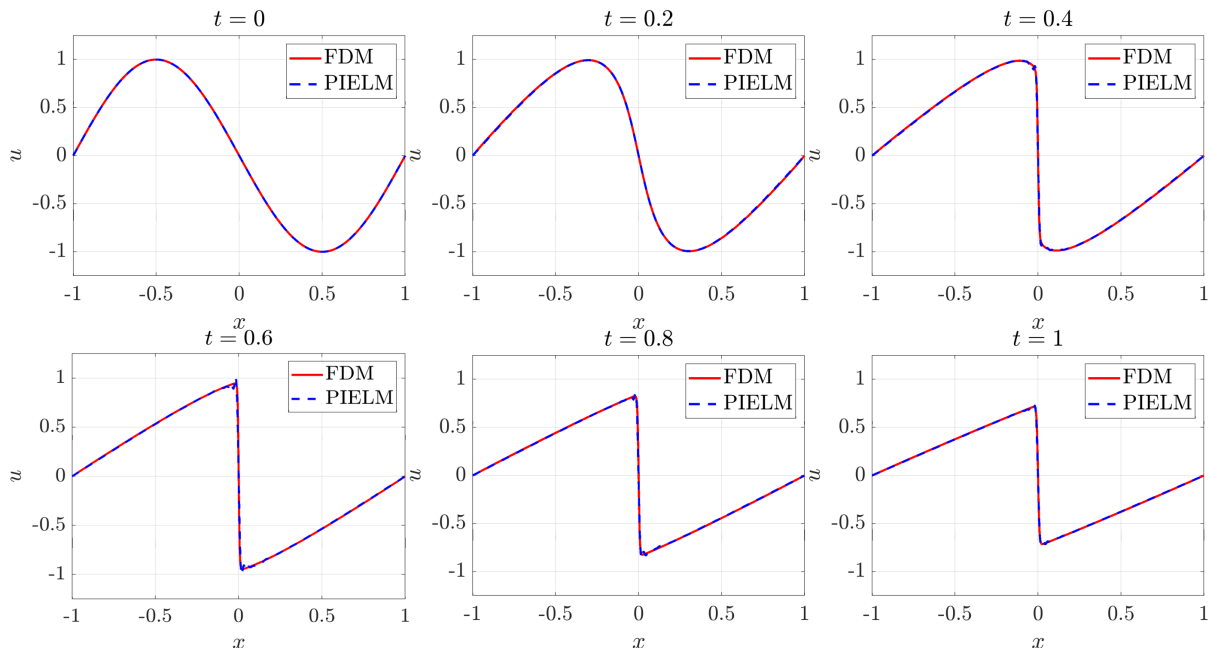


Figure 5: Temporal evolution of the PIELM solution for the viscous Burgers' equation allowing a standing shock.

	Travelling wave	Standing wave
Initial condition	$f(x) = e^{-30x^2}$	$f(x) = -\sin(\pi x)$
Viscosity	$0.01/\pi$	$0.01/\pi$
Data points per block	2113	2113
Parameters	1500	1500
Activation	RBF	RBF
Time blocks	1000	1000
Time taken	10.7 mins	13 mins

Table 3: PIELM solution details for Burgers' equation test cases.

Remarks

- In weakly nonlinear cases (i.e., for large values of ν), identifying high-gradient regions and concentrating sharp RBF kernels is not required. However, for shock cases, this step is essential; otherwise, the PIELM solution exhibits non-physical oscillations (see Figure 7), regardless of the number of sampling points or RBF kernels.
- Ideally, the size of the steep variation or shock region should be determined by the order of gradients and should vary with time. Likewise, the spread of the RBF kernels should also be time-dependent. However, in this study, the shock region width is kept fixed at 0.1 throughout the simulation. Consequently, we observe that PIELM performs better after the shock has fully developed compared to the early stages of its formation.
- In conventional time-marching methods, the time step size is governed by the spatial grid resolution through the CFL condition (Moura and Kubrusly, 2012). In our approach, effective shock resolution using PIELM requires a sufficient number of RBF centers and a carefully selected time step size. The precise mathematical criterion for determining these parameters remains an open question.
- Beyond spatio-temporal resolution, the stability of the PIELM solution is also influenced by the shape of the RBF kernels. If σ_t is too small in comparison to the size of the time step, the solution becomes unstable and diverges.

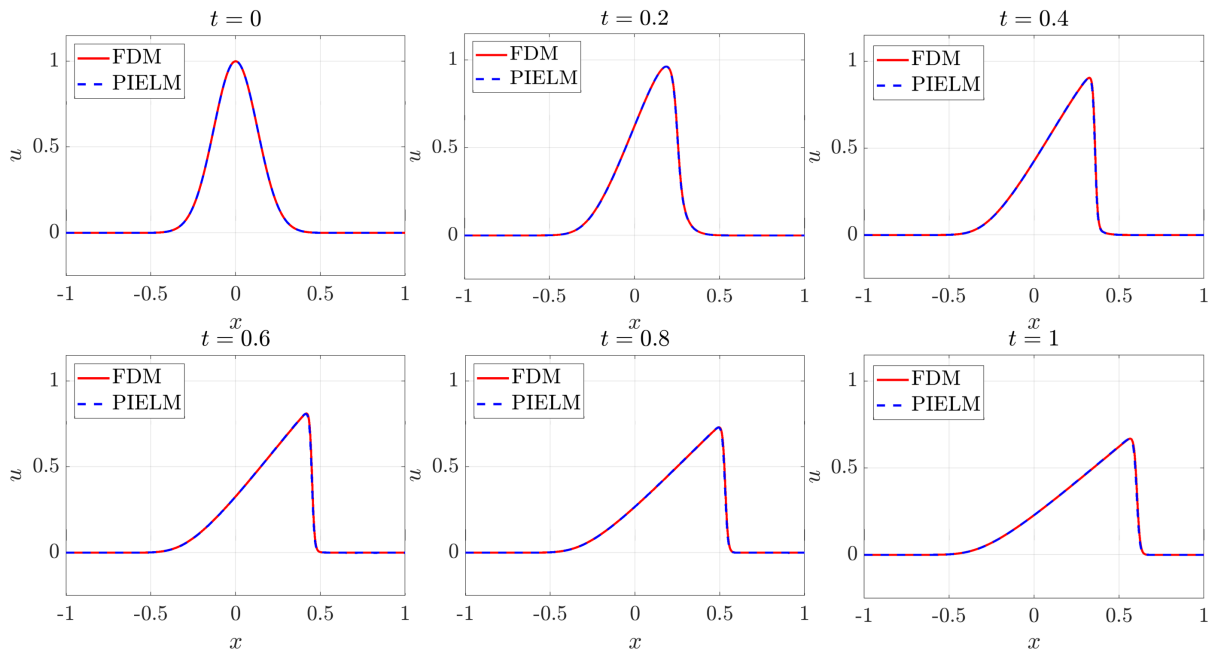


Figure 6: Temporal evolution of the PIELM solution for the viscous Burgers' equation allowing a travelling shock.

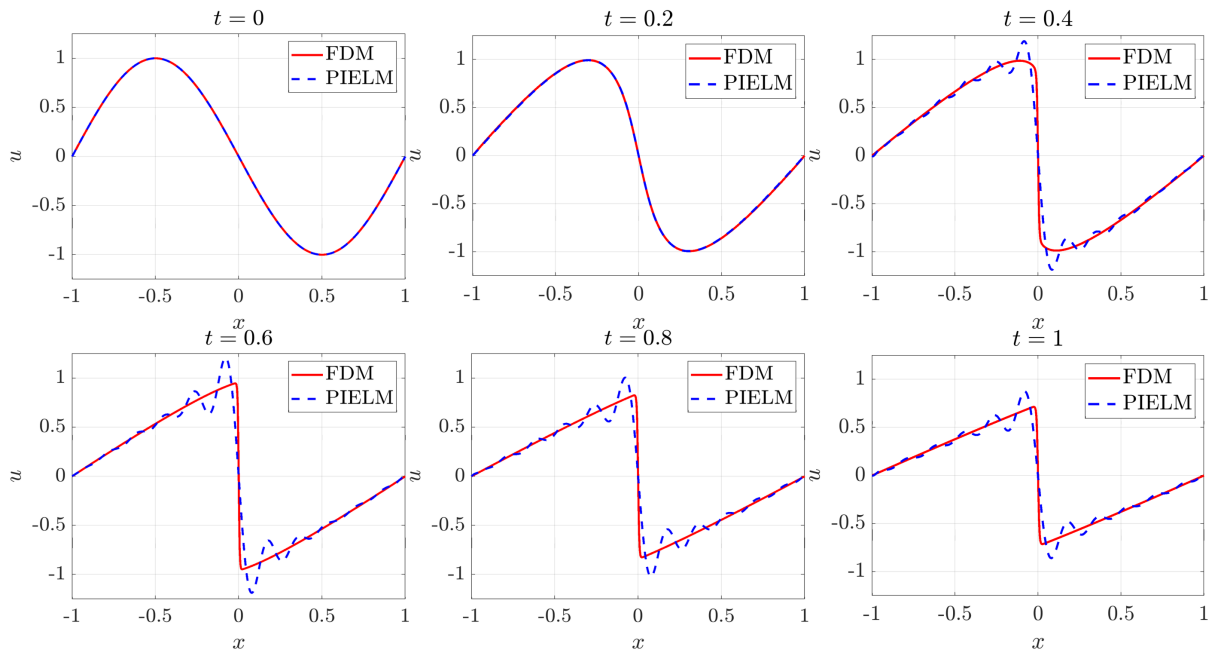


Figure 7: Unphysical oscillations in the PIELM solution for standing shock case.

4.3 Lid-Driven Cavity Flow

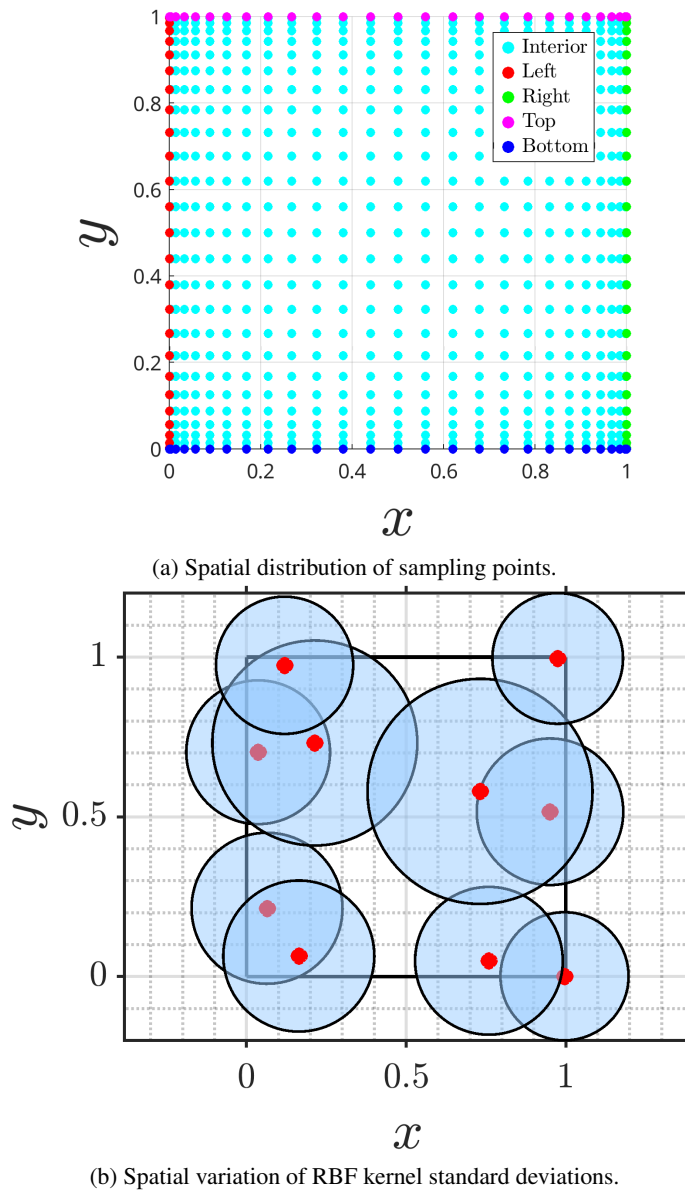


Figure 8: Sampling points distribution and RBF-kernel width variation for the lid-driven cavity flow.

In this section, we solve the classic lid-driven cavity problem (Marchi et al., 2009). The lid-driven cavity problem is a well-known benchmark in fluid dynamics for testing numerical methods that solve the incompressible Navier-Stokes equations. It consists of a unit-square cavity ($[0, 1] \times [0, 1]$) filled with a viscous, incompressible fluid, where the top lid moves at a constant horizontal velocity while the other three walls remain stationary. A no-slip boundary condition is applied, ensuring zero velocity at the walls except for the moving lid, which drives the flow inside the cavity. The fluid is assumed to be of unit density, and therefore the Reynolds number is given by $Re = 1/\nu$.

Mathematically, the governing system of PDEs are Navier-Stokes equations^{2,3} and the boundary conditions are expressed as follows:

- At the left edge, $\vec{V}(0, y) = (0, 0)$
- At the bottom edge, $\vec{V}(x, 0) = (0, 0)$
- At the right edge, $\vec{V}(1, y) = (0, 0)$

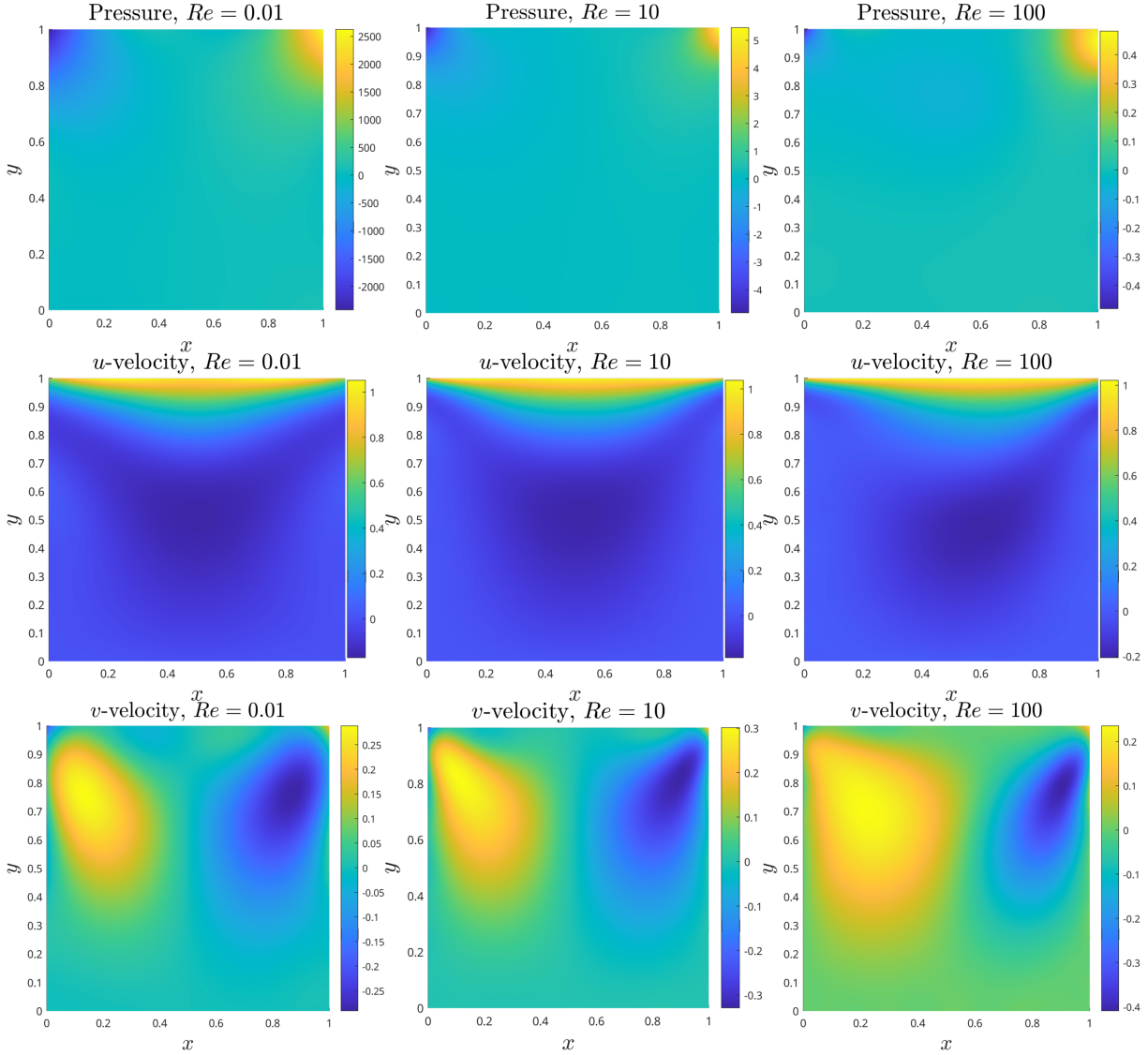


Figure 9: PIELM predicted velocity components and pressure for lid-driven cavity flow.

- At the top edge, $\vec{V}(x, 1) = (1, 0)$
- At the bottom left corner, $p(0, 0) = 0$

Figure 8 depicts the distribution of sampling points and spatial variation of RBF kernel widths. A total of 25×25 sampling points are used, arranged with Chebyshev spacing to concentrate more points near the walls for capturing sharp gradients. For PIELM, only 300 RBF kernels have been employed, as the lid-driven cavity flow remains laminar for Reynolds numbers up to 100. Similar to the sampling points, a denser placement of RBF kernels is maintained near the walls.

The standard deviation (σ) of the RBFs is determined based on their proximity to the boundaries, following the relation $\sigma = 0.2 + 0.4(L_{\min}/L_{\max})$, where L_{\min} denotes the minimum distance of an RBF center from the boundary walls, and L_{\max} is the maximum possible distance. For a unit square domain, $L_{\max} = 0.7071$. Compared to a random selection of σ , our choice of PIELM parameters is intuitive and entirely based on physical aspects of the problem.

The lid-driven cavity flow problem has previously been solved by PIELM using the vorticity-streamfunction approach for Stokes flow (Dwivedi and Srinivasan, 2020b). To our knowledge, this is the first attempt to solve it with PIELM in terms of (u, v, p) up to a Reynolds number of 100. Figure 9 presents the PIELM solutions for velocity components

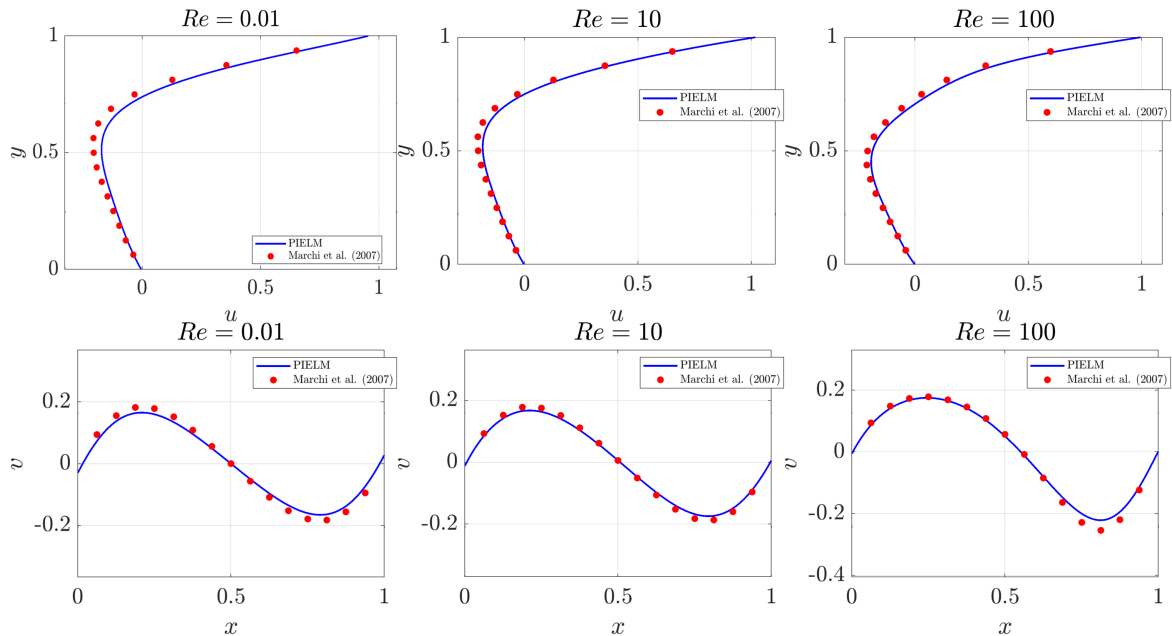


Figure 10: Comparison of centerline velocities with high resolution finite volume simulations (Marchi et al., 2009) for lid-driven cavity flow.

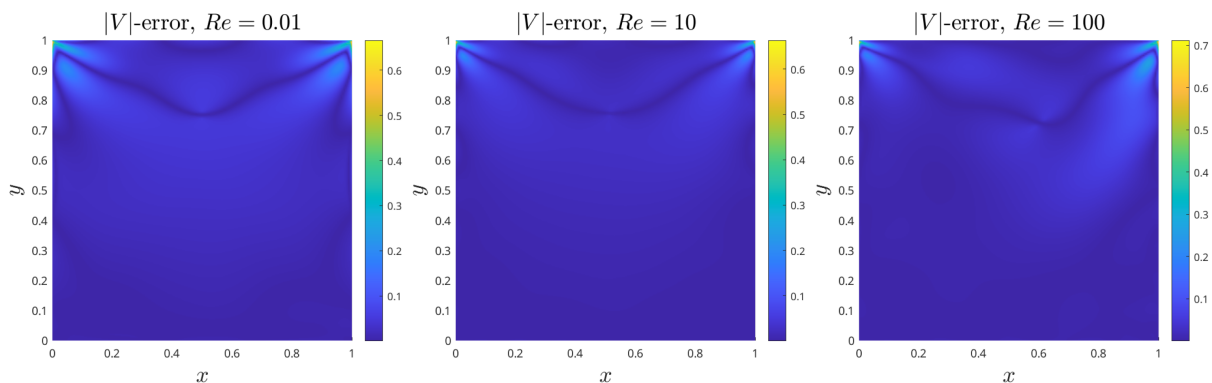


Figure 11: Error distribution of velocity magnitude at $Re = 0.01, 10, 100$

and pressure at $Re = 0.01, 10, 100$. To evaluate the accuracy of PIELM, we compare our results with an established reference. Since an exact analytical solution for the lid-driven cavity problem is unavailable, we use high-resolution finite-volume simulations from Marchi et al. (Marchi et al., 2009) as a benchmark.

Figure 10 illustrates the velocity profiles along the horizontal and vertical centerlines of the square, comparing the PIELM predictions with the well-established results of Marchi et al. (Marchi et al., 2009) at $Re = 0.01, 10, 100$. The comparison confirms that PIELM accurately captures the centerline velocity distributions, demonstrating its effectiveness in solving the lid-driven cavity problem. Figure 12 shows the effect of number of PIELM parameters on the results. The error in PIELM solutions decreases as we increase the number of neurons from 300 to 600 but this drop saturates and does not converge to zero by merely increasing the number of hidden-layer neurons.

To further analyze the error distribution across the domain, we compare the PIELM solution with the finite element-based solver FEniCS (Logg and Wells, 2010) on a high-resolution (250×250) mesh. The FEM implementation used for this comparison is available online⁵.

⁵https://github.com/cpraveen/fenics/blob/master/2d/ns_cavity/demo_steady.py

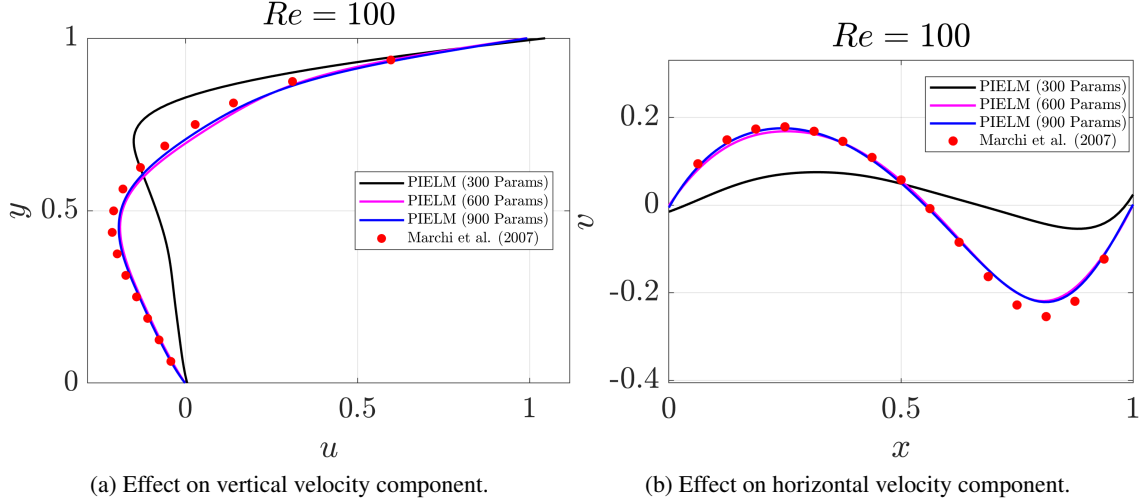


Figure 12: Effect of number of PIELM parameters on centerline velocity prediction.

The root mean square errors (RMSE) for the velocity magnitude are 0.039 at $Re = 0.01$, 0.026 at $Re = 10$ and 0.034 at $Re = 100$, with the corresponding error distributions shown in Figure 11. As expected, the highest errors occur near the top-left and top-right corners, where velocity discontinuities are present.

At first glance, it may seem counterintuitive that the RMSE at $Re = 100$ is lower than at $Re = 0.01$. However, as discussed in the second remark of the previous section, this behavior arises because the standard deviation of the RBF kernels is not adaptive and remains fixed across different Reynolds numbers.

For comparison with PINNs, we refer to a recent advanced variant called SPINN (Ramabathiran and Ramachandran, 2021). A comparison with SPINN reveals the computational efficiency of PIELM. For the lid-driven cavity problem at $Re = 100$, PIELM demonstrated superior performance, utilizing only 900 learnable parameters and completing the computation in 130 seconds. In contrast, SPINN required approximately 820 seconds to solve the same problem. This significant difference in computation time highlights PIELM's substantial speed advantage over PINN-based solvers.

For the lid-driven cavity problem up to $Re = 100$, a Reynolds number step size of 0.1 was used. However, applying the same step size up to $Re = 400$ results in inaccuracies in the PIELM solution. At this higher Reynolds number, the flow becomes advection-dominated, forming two secondary vortices near the bottom corners. Capturing these features requires more data points, additional neurons, and a reduced Reynolds number step size. However, determining the optimal values for these parameters remains an open question.

4.4 Stenotic Flow

Stenosis refers to the narrowing of a blood vessel, resulting in an increase in blood velocity in the stenotic throat due to the reduced cross-sectional area. Understanding blood flow in stenotic vessels is crucial in cardiovascular research, as it plays an important role in the development and progression of various cardiovascular diseases. Computational fluid dynamics (CFD) simulations provide a detailed analysis of flow patterns under different physiological conditions, such as rest and exercise. These simulations can also capture the effects of pulsatile flow and complex stenotic geometries.

In this section, we test PIELM to model blood flow in a stenotic vessel by solving the steady-state Navier-Stokes equations 2 and 3. Figure 13 depicts the computational geometry along with the distribution of sampling points. It also shows the spatial variation of RBF-kernel widths. The stenotic vessel has a total length of 1 unit ($L = 1$), with an inlet width of 0.1 unit ($R_{in} = 0.1$) and a constriction width of 0.06 unit ($D_c = 0.06$). The geometry is symmetric, with both the inlet and outlet extending 0.2 units.

To effectively capture flow dynamics, sampling points are distributed exponentially, ensuring a higher density near the throat. The placement of RBF centers follows the same principle. The standard deviation (σ) of the RBFs is determined based on their proximity to the boundaries, following the relation $\sigma = \min(D_c, 0.02 + D_c(L_{min}/D_c))$, where L_{min} denotes the minimum distance of an RBF center from the boundary walls. For this study, it is assumed that the fluid has a unit density ($\rho = 1$).

The boundary conditions are defined as follows. At the inlet, the velocity follows a parabolic profile:

$$\vec{V} = \begin{pmatrix} u \\ v \end{pmatrix} = \begin{pmatrix} U_{max} \left(1 - \left(\frac{y}{R_{in}} \right)^2 \right) \\ 0 \end{pmatrix} \quad (38)$$

where $U_{max} = 0.1$. No-slip conditions are imposed on the top and bottom walls, enforcing

$$\vec{V} = \begin{pmatrix} 0 \\ 0 \end{pmatrix}. \quad (39)$$

At the outlet, the pressure is set to zero ($p = 0$), and symmetric velocity boundary conditions are applied:

$$\frac{\partial u}{\partial x} = 0, \quad \frac{\partial v}{\partial x} = 0. \quad (40)$$

The Reynolds number is determined using the equation:

$$Re = \frac{\rho U_{max} R_{in}}{\mu} \quad (41)$$

To control the Reynolds number, we vary its value by adjusting the dynamic viscosity μ .

Figure 14 presents the PIELM-predicted solutions for stenotic flow at $Re = 10, 50,$ and 100 , while the corresponding FEM results are shown in Figure 15. The PIELM simulation employs 1000 PDE sampling points, 310 boundary points, and 2400 trainable parameters, whereas the FEM solution is computed using 13,959 total points and 27,124 triangular elements. The PIELM method accurately captures essential flow features, particularly the high velocity at the stenotic throat. The root mean square errors (RMSEs) between the PIELM and FEM solutions for velocity magnitude and pressure at $Re = 10, 50,$ and 100 are $(0.0053, 0.0267), (0.0054, 0.0071),$ and $(0.005, 0.003)$, respectively. As discussed in earlier sections, the counter-intuitive decrease in error with increasing Re is attributed to the fixed range of RBF spread across different values of Re .

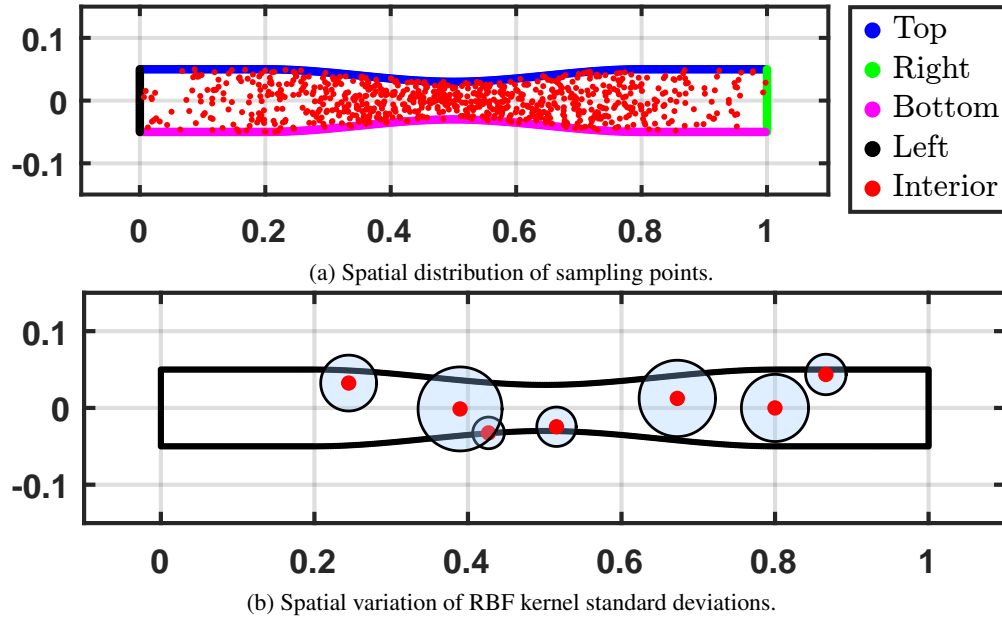


Figure 13: Sampling points distribution and RBF-kernel width variation for the stenotic flow.

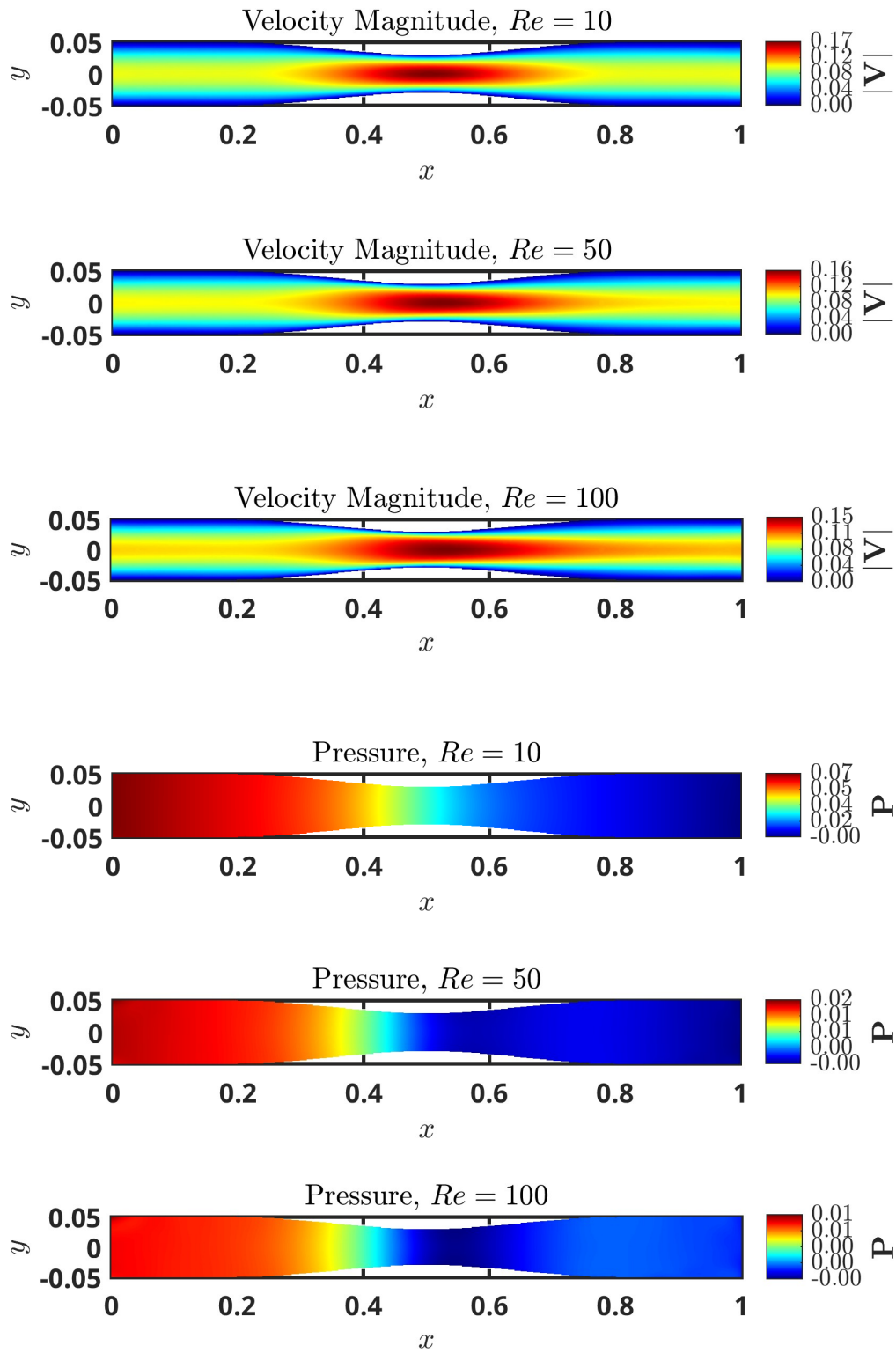


Figure 14: PIELM predicted solutions for the stenotic flow at $Re = 10, 50$ and 100 .

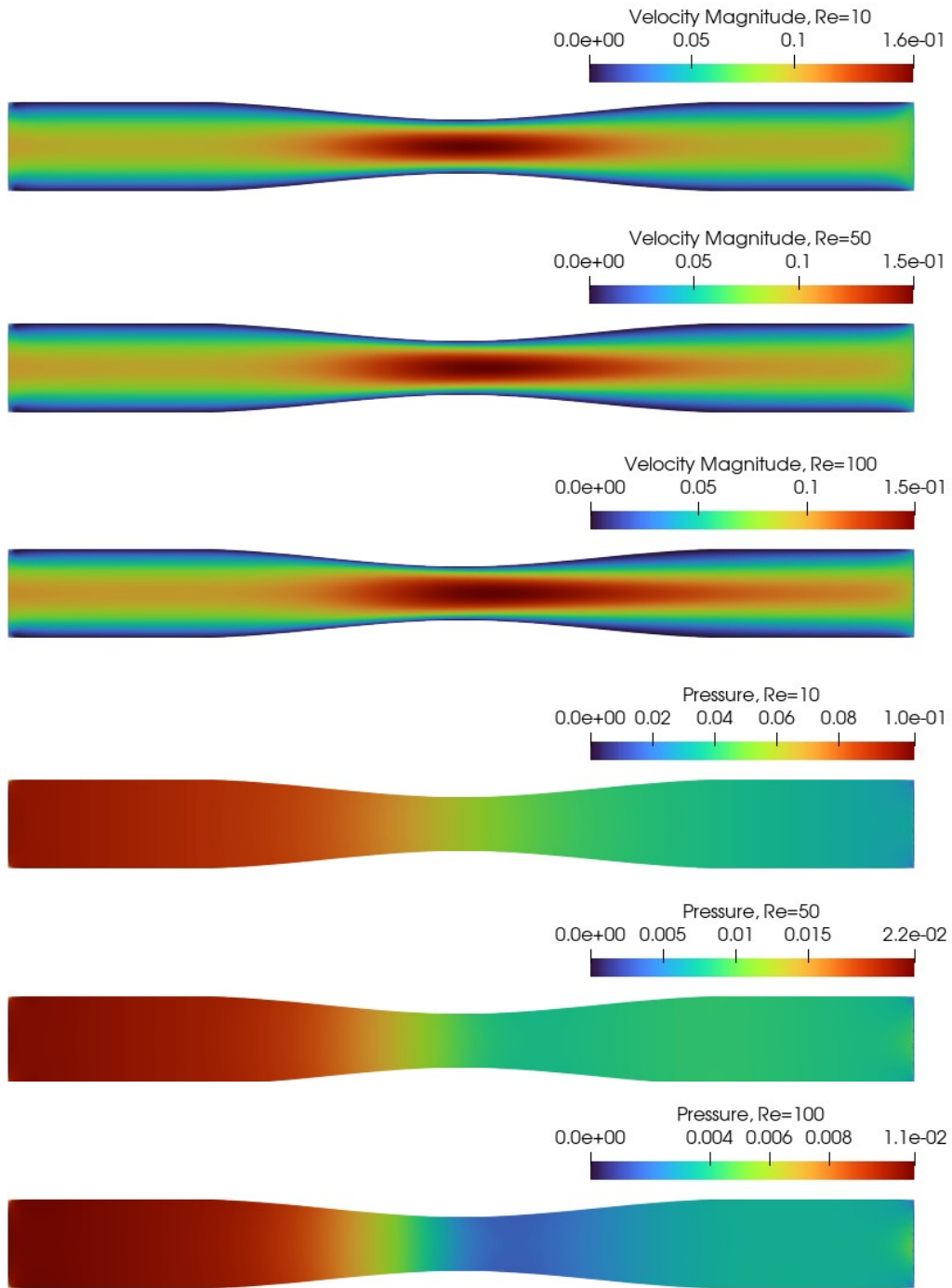


Figure 15: FEM solutions for the stenotic flow at $Re = 10, 50$ and 100 .

5 Conclusion

In this paper, we presented two physics-informed machine learning algorithms for solving nonlinear PDEs related to fluid flow by combining PIELM, curriculum learning, and RBF-kernels. While PIELMs are significantly faster than PINNs for linear PDEs, their direct application to nonlinear PDEs remains challenging. To overcome this, we integrated PIELMs with curriculum learning to solve nonlinear problems by iteratively solving their quasilinear approximations, tackling nonlinearity in a gradual and controlled manner. Building on the SPINN framework, we employed RBF kernels as activation functions, which establish a direct connection between PIELM function approximation and the RBF kernel collocation method, improving interpretability. We assessed the performance of curriculum-driven PIELMs on benchmark cases, including the Burgers' and Navier-Stokes equations, and analyzed their strengths and limitations. We also employed PIELM to simulate stenotic flow as a practical application. Based on our findings, we highlight the following key conclusions:

1. Interpretable PIELMs guided by curriculum learning were formulated to solve both steady and unsteady nonlinear PDEs.
2. A clear physical meaning is associated with the input layer parameters of the proposed PIELMs, corresponding to the centers and standard deviations of RBF kernels.
3. To the best of our knowledge, this study is the first in which PIELM has been applied to:
 - Solve Burgers' equation for traveling and standing shock cases.
 - Solve Navier-Stokes equations up to $Re = 100$ using a primary variable formulation.
4. The proposed PIELMs demonstrate a significant speed advantage over PINNs when solving weakly nonlinear PDEs. For example, while SPINN, a state-of-the-art PINN variant, takes 13 minutes to solve the lid-driven cavity flow at $Re = 100$, PIELM completes the same task in just 2 minutes.
5. The proposed PIELMs have been found to be comparable to PINNs in solving strongly nonlinear PDEs in terms of speed, while being more efficient in terms of the number of learnable parameters.
6. Unlike typical optimization algorithms where the training history lacks physical meaning, in this case, the iterations correspond to fluid flow at gradually increasing Reynolds numbers.
7. Beyond the benchmark cases, the curriculum learning-driven PIELM is employed to simulate stenotic flow as a practical application.

The proposed PIELM framework has potential applications in various areas, including microfluidics (Stokes flow, creeping flow), aerodynamics of small drones (low Reynolds number flows), incompressible internal flows (pipe and channel flows), groundwater and porous media flows, ocean and atmospheric flows (tidal currents, climate modeling), and biofluid dynamics (blood flow in large arteries). Future research will focus on expanding applications in these areas, and on automating PIELM hyperparameter selection.

References

- Bengio, Y. (2009). Learning deep architectures for ai.
- Bengio, Y., Louradour, J., Collobert, R., and Weston, J. (2009). Curriculum learning. In *Proceedings of the 26th Annual International Conference on Machine Learning, ICML '09*, page 41–48, New York, NY, USA. Association for Computing Machinery.
- Buhmann, M. D. (2000). *Radial basis functions*, volume 9. Cambridge university press.
- Calabrò, F., Fabiani, G., and Siettos, C. (2021). Extreme learning machine collocation for the numerical solution of elliptic pdes with sharp gradients. *Computer Methods in Applied Mechanics and Engineering*, 387:114188.
- Campos, D. (2021). Curriculum learning for language modeling.
- Canuto, C. G., Hussaini, M. Y., Quarteroni, A. M., and Zang, T. A. (2007). *Spectral Methods: Evolution to Complex Geometries and Applications to Fluid Dynamics (Scientific Computation)*. Springer-Verlag, Berlin, Heidelberg.
- Dong, S. and Li, Z. (2021). Local extreme learning machines and domain decomposition for solving linear and nonlinear partial differential equations. *Computer Methods in Applied Mechanics and Engineering*, 387:114129.
- Dong, S. and Yang, J. (2022). On computing the hyperparameter of extreme learning machines: Algorithm and application to computational pdes, and comparison with classical and high-order finite elements. *Journal of Computational Physics*, 463:111290.

- Dwivedi, V., Parashar, N., and Srinivasan, B. (2021). Distributed learning machines for solving forward and inverse problems in partial differential equations. *Neurocomputing*, 420:299–316.
- Dwivedi, V. and Srinivasan, B. (2020a). Physics informed extreme learning machine (pielm)—a rapid method for the numerical solution of partial differential equations. *Neurocomputing*, 391:96–118.
- Dwivedi, V. and Srinivasan, B. (2020b). Solution of biharmonic equation in complicated geometries with physics informed extreme learning machine. *Journal of Computing and Information Science in Engineering*, 20(6):061004.
- Elman, J. L. (1993). Learning and development in neural networks: The importance of starting small. *Cognition*, 48(1):71–99.
- Fasshauer, G. E. and Zhang, J. G. (2007). On choosing “optimal” shape parameters for rbf approximation. *Numerical Algorithms*, 45(1):345–368.
- Kansa, E. (1990a). Multiquadrics—a scattered data approximation scheme with applications to computational fluid-dynamics—i surface approximations and partial derivative estimates. *Computers and Mathematics with Applications*, 19(8):127–145.
- Kansa, E. (1990b). Multiquadrics—a scattered data approximation scheme with applications to computational fluid-dynamics—ii solutions to parabolic, hyperbolic and elliptic partial differential equations. *Computers and Mathematics with Applications*, 19(8):147–161.
- Karniadakis, G. E., Kevrekidis, I. G., Lu, L., Perdikaris, P., Wang, S., and Yang, L. (2021). Physics-informed machine learning. *Nature Reviews Physics*, 3(6):422–440.
- Krishnapriyan, A., Gholami, A., Zhe, S., Kirby, R., and Mahoney, M. W. (2021). Characterizing possible failure modes in physics-informed neural networks. In Ranzato, M., Beygelzimer, A., Dauphin, Y., Liang, P., and Vaughan, J. W., editors, *Advances in Neural Information Processing Systems*, volume 34, pages 26548–26560. Curran Associates, Inc.
- Logg, A. and Wells, G. N. (2010). DOLFIN: automated finite element computing. *ACM Transactions on Mathematical Software*, 37.
- Marchi, C. H., Suero, R., and Araki, L. K. (2009). The lid-driven square cavity flow: numerical solution with a 1024 x 1024 grid. *Journal of the Brazilian Society of Mechanical Sciences and Engineering*, 31:186–198.
- Moura, C. A. d. and Kubrusly, C. S. (2012). *The Courant-Friedrichs-Lewy (CFL) Condition: 80 Years After Its Discovery*. Birkhäuser Basel.
- Parisotto, E. and Salakhutdinov, R. (2017). Neural map: Structured memory for deep reinforcement learning. *arXiv preprint arXiv:1702.08360*.
- Raissi, M., Perdikaris, P., and Karniadakis, G. (2019). Physics-informed neural networks: A deep learning framework for solving forward and inverse problems involving nonlinear partial differential equations. *Journal of Computational Physics*, 378:686–707.
- Ramabathiran, A. A. and Ramachandran, P. (2021). Spinn: Sparse, physics-based, and partially interpretable neural networks for pdes. *Journal of Computational Physics*, 445:110600.
- Reddy, J. N. (2019). *Introduction to the Finite Element Method*. McGraw-Hill Education, New York, 4th edition edition.
- Versteeg, H. K. and Malalasekera, W. (2007). *An introduction to computational fluid dynamics the finite volume method, 2/E*. Pearson Education India.
- Wang, Y., Yue, Y., Lu, R., Han, Y., Song, S., and Huang, G. (2024). Efficienttrain++: Generalized curriculum learning for efficient visual backbone training. *IEEE Transactions on Pattern Analysis and Machine Intelligence (TPAMI)*.
- Zhang, W., Suo, W., Song, J., and Cao, W. (2024). Physics informed neural networks (pinns) as intelligent computing technique for solving partial differential equations: Limitation and future prospects.